nanomaterials

MDPI

Article

Efficient Hydrogen Evolution Reaction with Bulk and Nanostructured Mitrofanovite Pt_3Te_4

Gianluca D'Olimpio [1], Lixue Zhang [2], Chia-Nung Kuo [3,4], Daniel Farias [5,6,7], Luca Ottaviano [1,8], Chin Shan Lue [3,4], Jun Fujii [9], Ivana Vobornik [9], Amit Agarwal [10], Piero Torelli [9], Danil W. Boukhvalov [11,12] and Antonio Politano [1,13,14,*]

1 Department of Physical and Chemical Sciences, University of L'Aquila, Via Vetoio, 67100 L'Aquila, Italy; gianluca.dolimpio@univaq.it (G.D.); luca.ottaviano@aquila.infn.it (L.O.)
2 College of Chemistry and Chemical Engineering, Qingdao University, Qingdao 266071, China; zhanglx@qdu.edu.cn
3 Department of Physics, National Cheng Kung University, 1 Ta-Hsueh Road, Tainan 70101, Taiwan; kuochianung@gmail.com (C.-N.K.); cslue@ncku.edu.tw (C.S.L.)
4 Taiwan Consortium of Emergent Crystalline Materials, Ministry of Science and Technology, Taipei 10601, Taiwan
5 Departamento de Física de la Materia Condensada, Universidad Autónoma de Madrid, 28049 Madrid, Spain; daniel.farias@uam.es
6 Instituto "Nicolás Cabrera", Campus de Cantoblanco, 28049 Madrid, Spain
7 Condensed Matter Physics Center (IFIMAC), Universidad Autónoma de Madrid, 28049 Madrid, Spain
8 CNR-SPIN, Uos L'Aquila, Via Vetoio 10, 67100 L'Aquila, Italy
9 CNR-IOM, TASC Laboratory, Area Science Park-Basovizza, 34149 Trieste, Italy; jun.fujii@elettra.eu (J.F.); ivana.vobornik@elettra.eu (I.V.); piero.torelli@elettra.eu (P.T.)
10 Department of Physics, Indian Institute of Technology Kanpur, Kanpur 208016, India; amitag@iitk.ac.in
11 College of Science, Institute of Materials Physics and Chemistry, Nanjing Forestry University, Nanjing 210037, China; danil@njfu.edu.cn
12 Theoretical Physics and Applied Mathematics Department, Ural Federal University, Mira Street 19, 620002 Ekaterinburg, Russia
13 CNR-IMM, Istituto per la Microelettronica e Microsistemi, VIII Strada 5, 95121 Catania, Italy
14 INSTM, University of L'Aquila Unit, 67100 L'Aquila, Italy
* Correspondence: antonio.politano@univaq.it

Abstract: Here, we discuss the key features of electrocatalysis with mitrofanovite (Pt_3Te_4), a recently discovered mineral with superb performances in hydrogen evolution reaction. Mitrofanovite is a layered topological metal with spin-polarized topological surface states with potential applications for spintronics. However, mitrofanovite is also an exceptional platform for electrocatalysis, with costs of the electrodes suppressed by 47% owing to the partial replacement of Pt with Te. Remarkably, the Tafel slope in nanostructured mitrofanovite is just 33 mV/dec, while reduced mitrofanovite has the same Tafel slope (36 mV/dec) as state-of-the-art electrodes of pure Pt. Mitrofanovite also affords surface stability and robustness to CO poisoning. Accordingly, these findings pave the way for the advent of mitrofanovite for large-scale hydrogen production.

Keywords: metal chalcogenides; hydrogen evolution reaction; electrocatalysis

check for updates

Citation: D'Olimpio, G.; Zhang, L.; Kuo, C.-N.; Farias, D.; Ottaviano, L.; Lue, C.S.; Fujii, J.; Vobornik, I.; Agarwal, A.; Torelli, P.; et al. Efficient Hydrogen Evolution Reaction with Bulk and Nanostructured Mitrofanovite Pt_3Te_4. *Nanomaterials* **2022**, *12*, 558. https://doi.org/10.3390/nano12030558

Academic Editors: Molle Alessandro and Christian M. Julien

Received: 28 December 2021
Accepted: 2 February 2022
Published: 6 February 2022

Publisher's Note: MDPI stays neutral with regard to jurisdictional claims in published maps and institutional affiliations.

1. Introduction

In recent years, renewable sources have played a pivotal role in the context of energy production, constituting a valid alternative to nonrenewable energy sources now close to exhaustion [1–3]. On the other hand, renewable energy sources are inexhaustible and have a low environmental impact. Accordingly, the capability to meet world energy demand in a sustainable way, minimizing both dependence on the unstable fossil fuel market and associated emissions, is one of the main challenges of the 21st century.

In this context, hydrogen could play a key role in the future of energy devices and their related implications for economy [4–7]. Hydrogen is the most abundant light element

of the universe. Its combustion reaction has a high calorific value, with the production of only water, avoiding the formation of greenhouse gases. It should not be considered as an energy source, but rather as an energy carrier, that is, a compound capable of conveying energy from one form to another.

Energy produced from renewable sources through water splitting can be stored through the formation of chemical bonds that are formed by the splitting of the H_2O molecule [8,9]. Nowadays, 3% of the world's hydrogen production concerns the electrolysis of water. Produced hydrogen can be stored, transported, and for energy purposes it can be used in fuel cells with the purpose of producing electricity again.

The water splitting reaction is endothermic and therefore requires energy that can be supplied by the flow of an electric current through an electrochemical cell.

$$2H_2O\ (aq) + \text{Energy} \rightarrow 2H_2\ (g) + O_2\ (g) \quad (1)$$

Water splitting is a process consisting of two reactions, the hydrogen evolution reaction (HER) [10,11] and the oxygen evolution reaction (OER) in which two catalysts are required, one for the oxidation of water into O_2, and another for the reduction of protons to H_2.

In the cathodic part of Equation (1) HER takes place:

$$2H_2O + 2e^- \rightarrow H_2 + 2OH^- \quad (2)$$

$$2H^+ + 2e^- \rightarrow H_2 \quad (3)$$

In a basic and acidic electrolyte, respectively.

HER begins with the Volmer step, which involves the bond of hydrogen to the electrode at an adsorption site M:

$$M + H_2O + e^- \rightarrow MH_{ads} + OH^- \quad (4)$$

$$M + H^+ + e^- \rightarrow MH_{ads} \quad (5)$$

And it is completed with a desorption step that takes place through the Tafel reaction:

$$MH_{ads} \rightarrow 2M + H_2 \quad (6)$$

Or via Heyrovsky's reaction:

$$H_2O + MH_{ads} + e^- \rightarrow M + H_2 + OH^- \quad (7)$$

$$MH_{ads} + H^+ + e^- \rightarrow H_2 + M \quad (8)$$

Thus, HER is a reduction reaction (hydrogen goes from an oxidation state +1 to 0) so it will take place at the cathode.

Definitely, green hydrogen production has enormous potential in providing a cycle of use of sustainable energy and opening a new paradigm for different industrial sectors that today mainly depend on fossil fuels and for which decarbonization is challenging. Electrolytic production of hydrogen faces technological challenges to develop scalable methods with inferior energy consumption. The key point is to reduce the cost of raw materials used as electrocatalysts currently based on pure platinum (Pt). Thus, the production of high purity hydrogen requires low-cost electrocatalysts, with relatively low loading of noble metals in electrodes.

Despite the excellent performances of Pt in HER, the high cost (>30 US $/g) and the restricted obtainability of Pt make unavoidable the quest of economic and earth-abundant potential alternatives [12–15]. One possible solution is to reduce Pt content by using Pt-based alloys [14,16].

Considering its crucial technological relevance, the identification of efficient electrocatalysts for HER with high activity, cost-effectiveness, and long-term stability represents one of the most important open challenges in electrochemistry.

In particular, mitrofanovite is a recently discovered mineral [17], which was demonstrated to be a topological metal with spin-polarized surface states, with subsequent capabilities for applications in spintronics [18]. Nevertheless, recent findings from different groups highlight the huge potential of mitrofanovite for hydrogen production [19,20]. In this Feature Article, the main features of electrocatalysis with mitrofanovite are discussed, with a particular focus on the effects of dimensionality on the catalytic performances. Moreover, we provide a comparison with parental compounds to highlight the capabilities of mitrofanovite.

2. Materials and Methods

Single crystals of Pt_3Te_4 were grown from the self-flux method. The mixtures of high purity Pt foil and Te ingots with a molar ratio of 51:49 were placed in an alumina crucible and sealed into a quartz ampoule. The quartz ampule was heated to 1080 °C for 24 h, then slowly cooled at a rate of 1 °C/h up to 970 °C. The excess flux was separated by centrifugation.

Micro-Raman spectra were acquired with a He–Ne laser source (λ = 632.8 nm) with a LABRAM spectrometer equipped with an optical microscope with a 100x MPLAN with numerical aperture of 0.9. The system operates in a back-scattering configuration and all the measure were carried out at room temperature.

X-ray photoelectron spectroscopy (XPS) measurements were performed at the Advanced Photoelectric Experiments-HE (APE-HE) beamline of the Elettra synchrotron in Trieste, Italy. XPS spectra were acquired at room temperature and in normal emission with an Omicron EA125 hemispherical analyser.

Atomic force microscopy (AFM) images were acquired with a Digital D5000, Veeco system operating in Tapping-mode.

Theoretical methods to calculate HER and OER are reported in Section S1 of the Supporting Information.

High-resolution electron energy loss spectroscopy (HREELS) experiments were carried out with an Ibach-type spectrometer with an energy resolution of 0.5 eV. The primary electron beam energy was 4 eV. All spectra were taken at room temperature and in specular geometry, with an incident angle of 55° with respect to the sample normal.

The synchrotron X-ray diffraction (SXRD) patterns were collected from 100 to 480 K with the MYTHEN detector with 15 keV beam at beam line 09A, Taiwan Photon Source, National Synchrotron Radiation Research Center (NSRRC) in Hsinchu, Taiwan. The single crystal was pulverized and packed in a 0.1 mm borosilicate capillary to minimize the absorption effect. The capillary was kept spinning during data collection for powder averaging.

Electrochemical tests were carried out on a Bio-Logic VSP-300 electrochemical workstation with a typical three-electrode system, in which a bulk Pt_3Te_4 plate, a Pt wire and a saturated Ag/AgCl were used as the working electrode, the counter electrode, and the reference electrode, respectively. The inherent electrochemical behaviour of Pt_3Te_4 was in 0.05 M phosphate buffered saline electrolyte (pH 7.0) at a scan rate of 50 mV s^{-1}. For HER tests, the polarization curves were obtained using LSV in 0.5 M H_2SO_4 at a scan rate of 2 mV s^{-1}. The chronopotentiometric test was performed in 0.5 M H_2SO_4 at a potential of −0.053 V (vs RHE).

3. Results and Discussion

The crystal structure of Pt_3Te_4 was formed by two different alternate Pt_2Te_2 and $PtTe_2$ sublayers, bonded along the vertical direction by a combination of electrostatic and van der Waals non-covalent forces (Figure 1a–c). In the $PtTe_2$ (Pt_2Te_2) sublayer, one (two) Pt atomic layers is (are) sandwiched between two Te atomic layers. Specifically, mitrofanovite belongs to the R-3m (No.166) space group with calculated lattice parameters equal to a = 3.99 Å and c = 35.40 Å. The single crystal of Pt_3Te_4 displays three Raman active modes at ~107, 132, and 169 cm^{-1}, assigned to A_{1g}, 2LA(M) and E_g phonons, respectively (Figure 1d). To

identify the phase, we carried out SXRD experiments, using a synchrotron-based facility to reduce the broadening of peaks compared to in-house XRD systems. All diffraction peaks in Figure 1e match with the Pt_3Te_4 structure (ICSD # 41372). Our single crystals did not display any minimal trace of contamination, as demonstrated by the XPS survey acquired with synchrotron radiation to enhance surface sensitivity and energy resolution (Figure 1f).

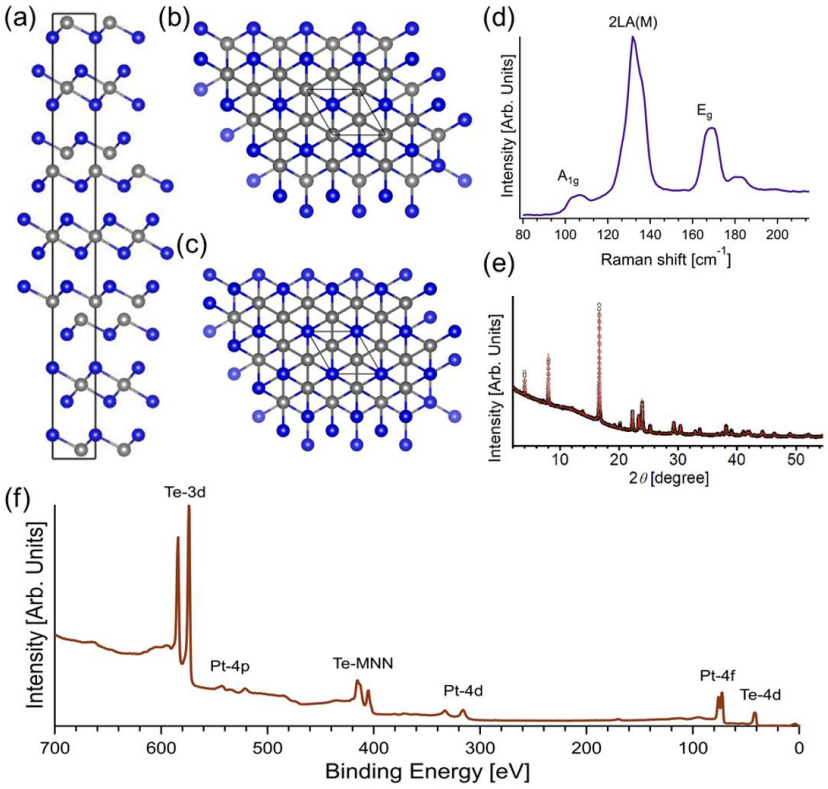

Figure 1. (**a**) Side view of Pt_3Te_4 crystal structure, with alternate $PtTe_2$ and Pt_2Te_2 layers stacked along the vertical direction. Panels (**b**,**c**) show the top view of Pt_3Te_4 with Pt_2Te_2 and $PtTe_2$ terminations, respectively. (**d**) Raman spectra acquired using a laser with λ = 632.8 nm. (**e**) SXRD pattern acquired at T = 300 K, together with the simulated SXRD pattern for Pt_3Te_4. (**f**) Survey spectrum of as-cleaved Pt_3Te_4 acquired with photons of 730 eV.

To study the surface chemical reactivity of single crystal Pt_3Te_4, we carried out synchrotron-based XPS experiments, whose superior energy resolution compared to standard XPS could unravel core-level shifts inaccessible with laboratory X-ray sources. Specifically, we studied the evolution of the surface chemical reactivity in oxygen and humid environment and finally in ambient atmosphere (Figure 2). The Pt-4f core level spectra was split into two components related to Pt-4f$_{7/2}$ and Pt-4f$_{5/2}$ shifted by 3.3 eV. The Pt-4f$_{7/2}$ component was characterized by two components located at binding energies (BEs) of 71.5 and 72.3 eV, respectively (Figure 2b). Actually, the presence of these two well-distinct spectral components was due to the $PtTe_2$ and Pt_2Te_2 sub-units [18]. The Te-3d core level was characterized by one doublet shifted by 10.4 eV, with the binding energy of Te-3d$_{5/2}$ peak of 573.1 eV (Figure 2a).

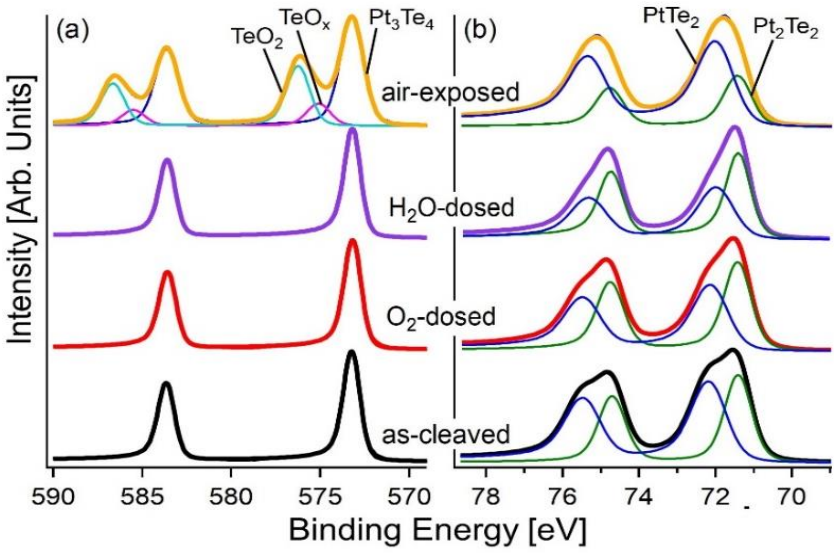

Figure 2. (**a**) Te-3d and (**b**) Pt-4f core level spectra of Pt_3Te_4 single crystal. The crystal was exfoliated in UHV to prevent oxidation and subsequently exposed to 10^4 L (1 L = 10^{-6} Torr·s) of oxygen (red spectra) and water (violet spectra). The yellow spectra represent the air exposed sample. The photon energy is 900 eV, all the spectra are normalized to the maximum.

After the modification of the surface towards 10^4 L of oxygen and water, no changes in the core levels of Pt and Te were observed. Only after air exposure did the Te-3d core level show the emergence of two new features with BEs of 575.7 and 573.8 eV for the J = 5/2 component, corresponding to TeO_2 and Te(0), respectively (Figure 2a). Moreover, the Te termination evolved into a nanometric oxide layer, whose thickness was estimated by quantitative XPS. Conversely, in the case of the Pt_3Te_4-nanocrystal, tellurium–oxide was always present [20].

Furthermore, the environmental stability of Pt_3Te_4 was studied through the analysis of the time evolution of AFM images (Figure 3a,b). In details, in Figure 3b the height profile along a specific direction remained constant during the air exposure, demonstrating that the morphology of the surface was unchanged. The relative stability of the surface of mitrofanovite made it a suitable candidate as an electrocatalyst.

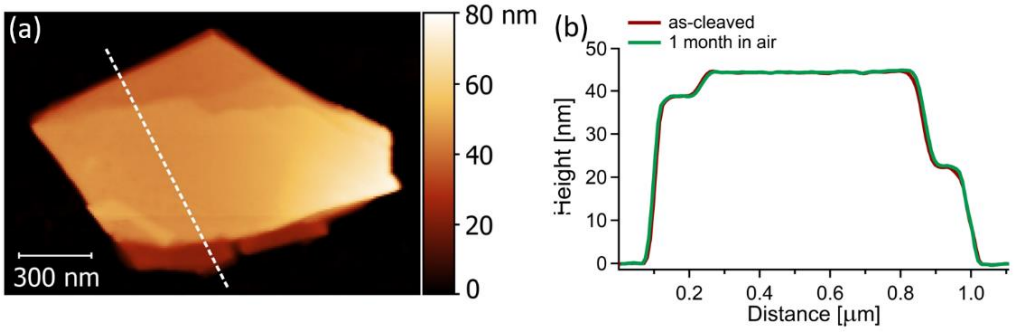

Figure 3. (**a**) AFM image of a 50 nm thick flake of Pt_3Te_4. (**b**) height profile taken along the dotted white line in (**a**).

Theoretical modelling indicates that physisorption and further decomposition of molecular oxygen were exothermic processes for both $PtTe_2$ and Pt_2Te_2 surfaces (Table 1). Step-by-step modelling of the oxidation process demonstrated that only Te atoms were oxidized on the surface layers of Pt_3Te_4 (Figure 4), in perfect agreement with the experimental results (Figure 2). Note that Pt centered on the surfaces of Pt_3Te_4 remained available for interaction with hydrogen even after oxidation.

Table 1. Differential enthalpy ΔH_{ads} and differential Gibbs free energy ΔG_{ads} for physical adsorption and differential enthalpy of decomposition ΔH_{dec} for molecular oxygen on $PtTe_2$- and Pt_2Te_2-terminated Pt_3Te_4 surfaces.

Adsorbent	SurfaceTermination	Site	ΔH_{ads} [kJ/mol]	ΔG_{ads} [kJ/mol]	ΔH_{dec} [kJ/mol]
O_2	$PtTe_2$	on-top	−42.7	−31.2	−51.8
		Te vacancy	−33.3	−22.0	−69.4
	Pt_2Te_2	on-top	−40.9	−29.6	−98.1
		Te vacancy	−35.0	−23.7	−163.0

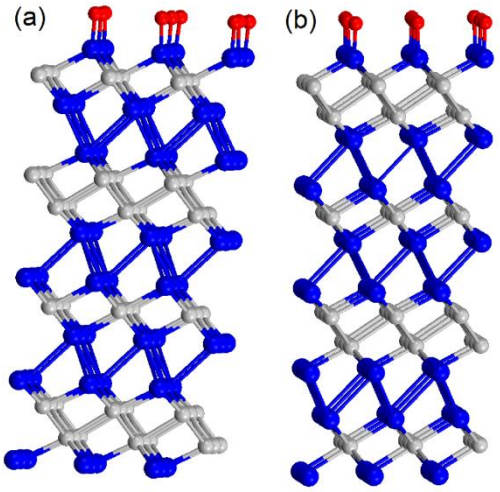

Figure 4. Optimized atomic structure of oxidized $PtTe_2$ (**a**) and Pt_2Te_2 (**b**) sides of Pt_3Te_4.

In Figure 5, we report the cyclic voltammetry tests by directly using Pt_3Te_4 bulk plate as the working electrode. Unlike $PtTe_2$, under neutral conditions, the evolution of hydrogen in Pt_3Te_4 becomes prominent for potential values below −1.35 V (vs. Ag/AgCl), while for $PtTe_2$, it is not prominent up to potential values below −1.8 V (vs. Ag/AgCl) [21,22], this reveals a very promising catalytic activity for Pt_3Te_4. Furthermore, in Figure 5, we show the cyclic voltammetry tests on the modified surface of Pt_3Te_4 to deeply study the heterogeneous electron transfer. Considering that Pt_3Te_4 undergoes redox behavior under different applied potentials, both the pristine Pt_3Te_4 and the same system modified by different electrochemical treatments were investigated. Herein, commonly used $[Fe(CN)_6]^{3-/4-}$ was selected as the redox probe. Definitely, both the oxidizing treatment (1.3 V (vs. Ag/AgCl) for 5 min) and reducing treatment (−1.5 V (vs. Ag/AgCl) for 5 min) had a positive effect and the cyclic voltammogram curves of $[Fe(CN)_6]^{3-/4-}$ on the pristine, oxidized, and reduced Pt_3Te_4 were similar. Remarkably, the electrochemical redox behavior of $[Fe(CN)_6]^{3-/4-}$ on the oxidized and reduced Pt_3Te_4 were even more reversible.

To compare the effectiveness of mitrofanovite for HER, we adopt as figures of merit (i) the Tafel slope (to assess kinetics at the electrode/electrolyte interface) and (ii) η10, i.e., the overpotential required to attain a cathodic current density of 10 mA cm^{-2} per geometric area. The Tafel slope estimates the potential increase necessary to increase the current density by one order of magnitude. In the case of an insufficient coverage of hydrogen atoms H_{ads}, the Volmer reaction would be the rate limiting step for the HER, resulting in a theoretical Tafel slope around 120 mV/dec. Conversely, for the highest values of H_{ads}, the HER-kinetic is dominated by the Heyrovsky or Tafel reaction, resulting in Tafel slopes around 30–40 mV/dec.

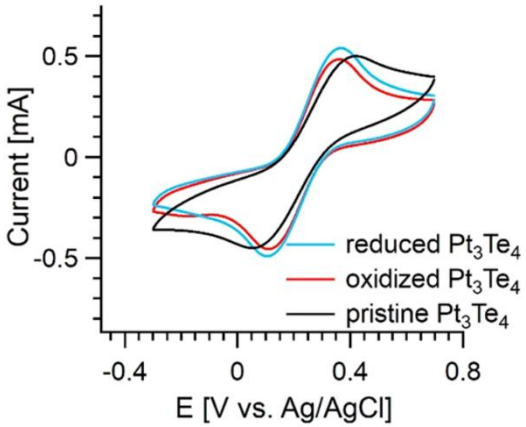

Figure 5. Cyclic voltammograms of the pristine and the electrochemically treated Pt_3Te_4 in 0.1 M KCl solution containing 5 mM $[Fe(CN)_6]^{3-/4-}$ at a scan rate of 50 mV s^{-1}. Reproduced with permission from Ref. [19].

In Figure 6, we compare the performances of mitrofanovite for HER with other Pt-based chalcogenides, such as PtS_2, $PtSe_2$, and $PtTe_2$. The pristine Pt_3Te_4 has a Tafel slope of ~49 mV/dec, while this value is modified in ~36 and 44 mV/dec for the reduced and oxidized surface of Pt_3Te_4, respectively. Note that the value of the Tafel slope in the reduced Pt_3Te_4 is comparable with the pristine Pt. Moreover, for all Pt_3Te_4 systems, including the oxidized surface, the Tafel slope is inferior to Pt-based dichalcogenides PtS_2, $PtSe_2$, and $PtTe_2$ (Figure 6a) [22–26] with a comparable value to those of Pt films and Pt/C [27]. Thus, the electrochemical treatment of the Pt_3Te_4 surface improves its performance as an electrocatalyst, and this can be correlated to an increase in the heterogeneous electron transfer capability. Additionally, from the inspection of Figure 6b it is evident that the Tafel slope of Pt_3Te_4 decreases with the dimensionality. In fact, in the case of Pt_3Te_4 nanocrystals, the reported Tafel slope was 33 mV/dec and the reported current density was as high as 7000 mA/cm^2, which should be attributed to the formation of numerous edges and defects in the growth process and the consequent near-zero Gibbs free-energy change of hydrogen adsorption [20].

Moreover, unlike other transition-metal dichalcogenides (TMDs) with high performance in HER and low current densities of 10–100 mA/cm^2, Pt_3Te_4 exhibits an overall current density, which exceeded 1000 mA/cm^2, i.e., a large value enabling in principle large-scale hydrogen production [28–31].

Notably, vibrational data (Figure 7) demonstrated that Pt_3Te_4 showed outstanding tolerance to CO (contrary to pure Pt, which suffers CO poisoning) and stability in a water environment, with subsequent high suitability for HER in both acidic and alkaline conditions. Physisorption of CO on Te vacancies was even more energetically unfavorable than on defects-free surfaces (+3.74 and +6.76 kJ/mol for the $PtTe_2$ and Pt_2Te_2 terminations of the Pt_3Te_4 surface, respectively).

To validate robustness to CO poisoning, we carried out high-resolution electron energy loss spectroscopy experiments, which is especially sensitive to CO adsorption (see our review for CO adsorption on catalytic surfaces [32] for more details), due to the high oscillating dipole. We carried out the experiment in specular conditions in order to maximize the sensitivity to dipole oscillations. Explicitly, we dosed CO onto (i) Pt_3Te_4(001); (ii) $PtTe_2$(001); (iii) Ni(111); (iv) Pt_3Ni(111); and (v) Pt(111) surfaces. We obtained that, while Ni(111), Pt_3Ni(111) and Pt(111) are poisoned by CO, as evidenced by the observation of C-O stretching and the CO-substrate vibrations, $PtTe_2$ and Pt_3Te_4 are totally inert toward CO, even after prolonged CO exposure up to 10^{10} L (Figure 7).

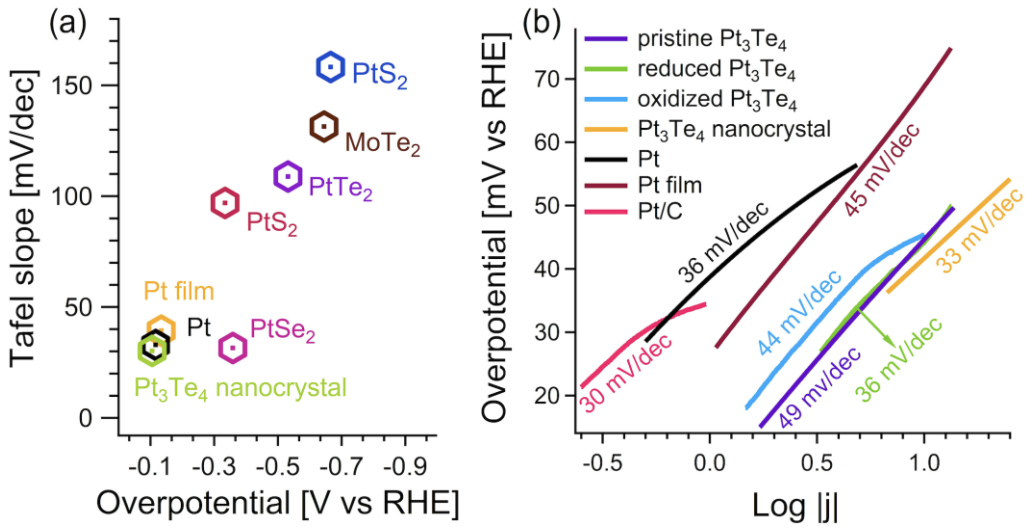

Figure 6. (**a**) Tafel slope vs overpotential for Pt_3Te_4 [19,20], $MoTe_2$ [20], Pt film [20], platinum dichalcogenides [22–25], platinum [27], and Pt/C [19]. (**b**) Comparison of Tafel plots for different Pt_3Te_4 crystals. Purple, green, light blue, and yellow lines represent pristine Pt_3Te_4, reduced Pt_3Te_4, oxidized Pt_3Te_4, and Pt_3Te_4 nanocrystals, respectively. For the sake of comparison, we also report Pt (black), Pt film (violet) and Pt/C (magenta). The figure is built using data from Refs. [19,20], and the spectra was renormalized to simplify the visualization.

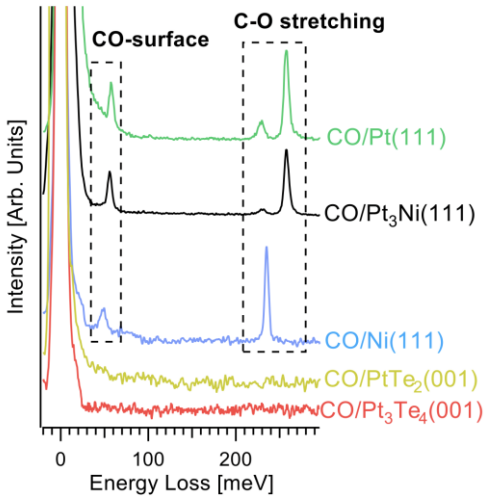

Figure 7. Vibrational spectra after having saturated with CO the surfaces of Pt_3Te_4(001), $PtTe_2$(001), Ni(111), Pt_3Ni(111) and Pt(111). The saturation has been reached at only 5, 10, and 8 L for Ni(111), Pt_3Ni(111), and Pt(111). On the other hand, no CO-derived features are achieved even after exposure to 1010 L on Pt_3Te_4(001) and $PtTe_2$(001). Specifically, the CO-derived features are the vibration of the whole CO molecule against the substrate at 50 meV [32,33] and the intramolecular C-O stretching [32], whose energy depends on the adsorption site: 230 meV for three-fold site, selectively occupied on Ni, while it is a minority on Pt_3Ni(111) and Pt(111), and 250 meV for the on-top adsorption site, a majority on both Pt_3Ni(111) and Pt(111).

To obtain more information on the stability of Pt_3Te_4 electrodes in the electrochemical environment, Pt-4f (Figure 8a) and Te-3d (Figure 8b) core levels were measured on both as-prepared and postmortem electrodes. From the inspection of Figure 8, it is quite evident that Pt_3Te_4 electrodes were not affected by degradation after electrochemical treatment, with just negligible changes. The only change is in the Te core level where we observe a lower component of tellurium oxide after the reaction. On the other hand, the electrochemical stability is a crucial aspect in electrocatalysis. The chronopotentiometric curve (Figure 8c)

in 0.5 M H_2SO_4 at a potential of −0.053 V vs RHE, showing negligible attenuation in a timescale extended up to three days further validates the outstanding chemical and electrocatalytic stability of Pt_3Te_4.

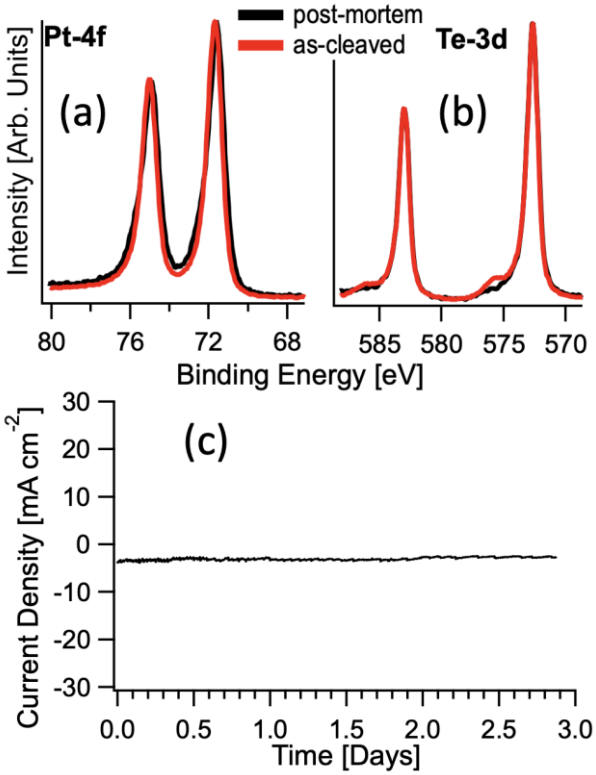

Figure 8. (**a**) Te-3d and (**b**) Pt-4f core level spectra of Pt_3Te_4 single crystal for as-prepared and postmortem electrodes. (**c**) Chronopotentiometric curve for bulk Pt_3Te_4 in 0.5 M H_2SO_4 at a potential of −0.053 V vs. RHE.

4. Conclusions

In this paper, we discussed the key features ruling electrocatalysis with mitrofanovite (Pt_3Te_4), a recently discovered mineral with superb performances in HER.

Mitrofanovite has a surface stable even upon exposure to ambient atmosphere, with just a sub-nanometric oxide skin.

Mitrofanovite represents an exceptional platform for electrocatalysis, with costs of the electrodes suppressed by 47% owing to the partial replacement of Pt with Te. Remarkably, the Tafel slope in nanostructured mitrofanovite is just 33 mV/dec, while reduced mitrofanovite has the same Tafel slope (36 mV/dec) than state-of-the-art electrodes of pure Pt. Contrary to Pt, mitrofanovite is not affected by CO poisoning.

Accordingly, these results pave the way for the advent of mitrofanovite for large-scale hydrogen production.

Supplementary Materials: The following supporting information can be downloaded at: https://www.mdpi.com/article/10.3390/nano12030558/s1, Section S1: Theoretical Methods. Refs. [34–39].

Author Contributions: Conceptualization, D.W.B., A.A., I.V. and A.P.; methodology, I.V., J.F., A.A. and C.S.L.; software, G.D., D.W.B. and A.P.; validation, D.F., G.D. and P.T.; formal analysis, G.D. and P.T.; investigation, P.T., L.Z., G.D., J.F. and C.-N.K.; resources, A.P., D.F. and C.S.L.; data curation, G.D.; writing—original draft preparation, G.D. and A.P.; writing—review and editing, D.W.B. and A.P.; visualization, D.W.B., G.D. and A.P.; supervision, A.P.; project administration, A.P. and D.F.; funding acquisition, I.V., L.O. and D.F. All authors have read and agreed to the published version of the manuscript.

Funding: D.W.B. acknowledges support from the Ministry of Science and Higher Education of the Russian Federation (through the basic part of the government mandate, Project No. FEUZ-2020–0060) and the Jiangsu Innovative and Entrepreneurial Talents Project. This work has been partially supported by the Spanish Ministerio de Ciencia e Innovación under Project PID2019–109525RB-I00. D.F. acknowledges financial support from the Spanish Ministry of Economy and Competitiveness, through the "Maríade Maeztu" Programme for Units of Excellence in R&D (CEX2018-000805-M). I.V., J. F., and P.T. thank NFFA-Trieste.

Data Availability Statement: Data are available pending reasonable requests to the corresponding authors.

Conflicts of Interest: The authors declare no conflict of interest.

References

1. Lu, Y.; Khan, Z.A.; Alvarez-Alvarado, M.S.; Zhang, Y.; Huang, Z.; Imran, M. A critical review of sustainable energy policies for the promotion of renewable energy sources. *Sustainability* **2020**, *12*, 5078. [CrossRef]
2. Al-Shetwi, A.Q.; Hannan, M.; Jern, K.P.; Mansur, M.; Mahlia, T. Grid-connected renewable energy sources: Review of the recent integration requirements and control methods. *J. Clean. Prod.* **2020**, *253*, 119831. [CrossRef]
3. Kim, C.; Lee, S.; Kim, S.H.; Park, J.; Kim, S.; Kwon, S.H.; Bae, J.S.; Park, Y.S.; Kim, Y. Cobalt–iron–phosphate hydrogen evolution reaction electrocatalyst for solar-driven alkaline seawater electrolyzer. *Nanomaterials* **2021**, *11*, 2989. [CrossRef] [PubMed]
4. Juodkazytė, J.; Juodkazis, K.; Juodkazis, S. Atoms vs. Ions: Intermediates in Reversible Electrochemical Hydrogen Evolution Reaction. *Catalysts* **2021**, *11*, 1135. [CrossRef]
5. Evangelista, A.J.; Ivanchenko, M.; Jing, H. Efficient near-infrared-activated photocatalytic hydrogen evolution from ammonia borane with core-shell upconversion-semiconductor hybrid nanostructures. *Nanomaterials* **2021**, *11*, 23237. [CrossRef]
6. Guo, Y.; Xu, A.; Hou, J.; Liu, Q.; Li, H.; Guo, X. Ag–Au core–shell triangular nanoprisms for improving p-g-C_3N_4 photocatalytic hydrogen production. *Nanomaterials* **2021**, *11*, 23347. [CrossRef] [PubMed]
7. Jo, S.G.; Kim, C.S.; Kim, S.J.; Lee, J.W. Phase-controlled NiO nanoparticles on reduced graphene oxide as electrocatalysts for overall water splitting. *Nanomaterials* **2021**, *11*, 23379. [CrossRef]
8. Sun, L.; Li, Y.; Feng, W. Gas-phase fluorination of g-C_3N_4 for enhanced photocatalytic hydrogen evolution. *Nanomaterials* **2022**, *12*, 10037. [CrossRef]
9. Wang, K.; Zhang, J.; Ye, Y.; Ma, H.; Liu, B.; Zhang, P.; Xu, B. Facile synthesis of 1T-phase MoS_2 nanosheets on n-doped carbon nanotubes towards highly efficient hydrogen evolution. *Nanomaterials* **2021**, *11*, 3273. [CrossRef]
10. Ďurovič, M.; Hnát, J.; Bouzek, K. Electrocatalysts for the hydrogen evolution reaction in alkaline and neutral media. A comparative review. *J. Power Sources* **2021**, *493*, 229708. [CrossRef]
11. Pu, Z.; Amiinu, I.S.; Cheng, R.; Wang, P.; Zhang, C.; Mu, S.; Zhao, W.; Su, F.; Zhang, G.; Liao, S. Single-atom catalysts for electrochemical hydrogen evolution reaction: Recent advances and future perspectives. *Nano-Micro Lett.* **2020**, *12*, 1–29. [CrossRef]
12. Boukhvalov, D.W.; Edla, R.; Cupolillo, A.; Fabio, V.; Sankar, R.; Zhu, Y.; Mao, Z.; Hu, J.; Torelli, P.; Chiarello, G.; et al. Surface Instability and Chemical Reactivity of ZrSiS and ZrSiSe Nodal-Line Semimetals. *Adv. Funct. Mater.* **2019**, *29*, 1900438. [CrossRef]
13. Gao, J.; Cupolillo, A.; Nappini, S.; Bondino, F.; Edla, R.; Fabio, V.; Sankar, R.; Zhang, Y.W.; Chiarello, G.; Politano, A. Surface Reconstruction, Oxidation Mechanism, and Stability of Cd_3As_2. *Adv. Funct. Mater.* **2019**, *29*, 1900965. [CrossRef]
14. Politano, A.; Chiarello, G.; Kuo, C.-N.; Lue, C.S.; Edla, R.; Torelli, P.; Pellegrini, V.; Boukhvalov, D.W. Tailoring the Surface Chemical Reactivity of Transition-Metal Dichalcogenide $PtTe_2$ Crystals. *Adv. Funct. Mater.* **2018**, *28*, 1706504. [CrossRef]
15. Politano, A.; Chiarello, G.; Li, Z.; Fabio, V.; Wang, L.; Guo, L.; Chen, X.; Boukhvalov, D.W. Toward the effective exploitation of topological phases of matter in catalysis: Chemical reactions at the surfaces of NbAs and TaAs Weyl semimetals. *Adv. Funct. Mater.* **2018**, *28*, 1800511. [CrossRef]
16. Huang, X.; Zhao, Z.; Cao, L.; Chen, Y.; Zhu, E.; Lin, Z.; Li, M.; Yan, A.; Zettl, A.; Wang, Y.M.; et al. High-performance transition metal–doped Pt_3Ni octahedra for oxygen reduction reaction. *Science* **2015**, *348*, 1230–1234. [CrossRef] [PubMed]
17. Subbotin, V.V.; Vymazalová, A.; Laufek, F.; Savchenko, Y.E.; Stanley, C.J.; Gabov, D.A.; Plášil, J. Mitrofanovite, Pt_3Te_4, a new mineral from the East Chuarvy deposit, Fedorovo-Pana intrusion, Kola Peninsula, Russia. *Mineral. Mag.* **2019**, *83*, 523–530. [CrossRef]
18. Fujii, J.; Ghosh, B.; Vobornik, I.; Bari Sarkar, A.; Mondal, D.; Kuo, C.N.; Bocquet, F.C.; Zhang, L.; Boukhvalov, D.W.; Lue, C.S.; et al. Mitrofanovite Pt_3Te_4: A Topological Metal with Termination-Dependent Surface Band Structure and Strong Spin Polarization. *ACS Nano* **2021**, *15*, 14786–14793. [CrossRef] [PubMed]
19. Boukhvalov, D.W.; Cheng, J.; D'Olimpio, G.; Bocquet, F.C.; Kuo, C.-N.; Sarkar, A.B.; Ghosh, B.; Vobornik, I.; Fujii, J.; Hsu, K.; et al. Unveiling the Mechanisms Ruling the Efficient Hydrogen Evolution Reaction with Mitrofanovite Pt_3Te_4. *J. Phys. Chem. Lett.* **2021**, *12*, 8627–8636. [CrossRef]
20. Bae, D.; Park, K.; Kwon, H.; Won, D.; Ling, N.; Baik, H.; Yang, J.; Park, H.J.; Cho, J.; Yang, H.; et al. Mitrofanovite, Layered Platinum Telluride, for Active Hydrogen Evolution. *ACS Appl. Mater. Interfaces* **2021**, *13*, 2437–2446. [CrossRef]

21. Chia, X.; Sofer, Z.; Luxa, J.; Pumera, M. Layered Noble Metal Dichalcogenides: Tailoring Electrochemical and Catalytic Properties. *ACS Appl. Mater. Interfaces* **2017**, *9*, 25587–25599. [CrossRef] [PubMed]
22. Chia, X.; Adriano, A.; Lazar, P.; Sofer, Z.; Luxa, J.; Pumera, M. Layered Platinum Dichalcogenides (PtS_2, $PtSe_2$, and $PtTe_2$) Electrocatalysis: Monotonic Dependence on the Chalcogen Size. *Adv. Funct. Mater.* **2016**, *26*, 4306–4318. [CrossRef]
23. Wang, Y.; Szokolova, K.; Nasir, M.Z.M.; Sofer, Z.; Pumera, M. Layered Crystalline and Amorphous Platinum Disulfide (PtS_2): Contrasting Electrochemistry. *Chem. Eur. J.* **2019**, *25*, 7330–7338. [CrossRef] [PubMed]
24. Hu, D.; Zhao, T.; Ping, X.; Zheng, H.; Xing, L.; Liu, X.; Zheng, J.; Sun, L.; Gu, L.; Tao, C.; et al. Unveiling the Layer-Dependent Catalytic Activity of $PtSe_2$ Atomic Crystals for the Hydrogen Evolution Reaction. *Angew. Chem. Int. Ed.* **2019**, *58*, 6977–6981. [CrossRef] [PubMed]
25. Lin, S.; Liu, Y.; Hu, Z.; Lu, W.; Mak, C.H.; Zeng, L.; Zhao, J.; Li, Y.; Yan, F.; Tsang, Y.H.; et al. Tunable active edge sites in $PtSe_2$ films towards hydrogen evolution reaction. *Nano Energy* **2017**, *42*, 26–33. [CrossRef]
26. Rosli, N.F.; Mayorga-Martinez, C.C.; Latiff, N.M.; Rohaizad, N.; Sofer, Z.; Fisher, A.C.; Pumera, M. Layered $PtTe_2$ Matches Electrocatalytic Performance of Pt/C for Oxygen Reduction Reaction with Significantly Lower Toxicity. *ACS Sustain. Chem. Eng.* **2018**, *6*, 7432–7441. [CrossRef]
27. Seok, J.; Lee, J.-H.; Cho, S.; Ji, B.; Kim, H.W.; Kwon, M.; Kim, D.; Kim, Y.-M.; Oh, S.H.; Kim, S.W.; et al. Active hydrogen evolution through lattice distortion in metallic $MoTe_2$. *2D Mater.* **2017**, *4*, 25061. [CrossRef]
28. Yang, J.; Mohmad, A.R.; Wang, Y.; Fullon, R.; Song, X.; Zhao, F.; Bozkurt, I.; Augustin, M.; Santos, E.J.G.; Shin, H.S.; et al. Ultrahigh-current-density niobium disulfide catalysts for hydrogen evolution. *Nat. Mater.* **2019**, *18*, 1309–1314. [CrossRef]
29. Mishra, I.K.; Zhou, H.; Sun, J.; Qin, F.; Dahal, K.; Bao, J.; Chen, S.; Ren, Z. Hierarchical CoP/Ni_5P_4/CoP microsheet arrays as a robust pH-universal electrocatalyst for efficient hydrogen generation. *Energy Environ. Sci.* **2018**, *11*, 2246–2252. [CrossRef]
30. Yu, F.; Zhou, H.; Huang, Y.; Sun, J.; Qin, F.; Bao, J.; Goddard, W.A.; Chen, S.; Ren, Z. High-performance bifunctional porous non-noble metal phosphide catalyst for overall water splitting. *Nat. Commun.* **2018**, *9*, 2551. [CrossRef]
31. Chen, Y.; Yu, G.; Chen, W.; Liu, Y.; Li, G.-D.; Zhu, P.; Tao, Q.; Li, Q.; Liu, J.; Shen, X.; et al. Highly Active, Nonprecious Electrocatalyst Comprising Borophene Subunits for the Hydrogen Evolution Reaction. *J. Am. Chem. Soc.* **2017**, *139*, 12370–12373. [CrossRef] [PubMed]
32. Politano, A.; Chiarello, G. Vibrational investigation of catalyst surfaces: Change of the adsorption site of CO molecules upon coadsorption. *J. Phys. Chem. C* **2011**, *115*, 13541–13553. [CrossRef]
33. Politano, A.; Formoso, V.; Agostino, R.G.; Colavita, E.; Chiarello, G. Influence of CO adsorption on the alkali-substrate bond studied by high-resolution electron energy loss spectroscopy. *Phys. Rev. B* **2007**, *76*, 233403. [CrossRef]
34. Giannozzi, P.; Baroni, S.; Bonini, N.; Calandra, M.; Car, R.; Cavazzoni, C.; Ceresoli, D.; Chiarotti, G.L.; Cococcioni, M.; Dabo, I. QUANTUM ESPRESSO: A modular and open-source software project for quantum simulations of materials. *J. Phys. Condens. Matter* **2009**, *21*, 395502.
35. Perdew, J.P.; Burke, K.; Ernzerhof, M. Generalized Gradient Approximation Made Simple. *Phys. Rev. Lett.* **1996**, *77*, 3865–3868. [CrossRef]
36. Barone, V.; Casarin, M.; Forrer, D.; Pavone, M.; Sambi, M.; Vittadini, A. Role and effective treatment of dispersive forces in materials: Polyethylene and graphite crystals as test cases. *J. Comput. Chem.* **2009**, *30*, 934–939. [CrossRef]
37. Monkhorst, H.J.; Pack, J.D. Special points for Brillouin-zone integrations. *Phys. Rev. B* **1976**, *13*, 5188–5192. [CrossRef]
38. Greeley, J.; Jaramillo, T.F.; Bonde, J.; Chorkendorff, I.; Nørskov, J.K. Computational high-throughput screening of electrocatalytic materials for hydrogen evolution. *Nat. Mater.* **2006**, *5*, 909–913. [CrossRef]
39. Tang, Y.; Allen, B.L.; Kauffman, D.R.; Star, A. Electrocatalytic activity of nitrogen-doped carbon nanotube cups. *J. Am. Chem. Soc.* **2009**, *131*, 13200–13201. [CrossRef]